Physics of Fluids

Effects of phase difference on hydrodynamic interactions and wake patterns in high-density fish schools

Cite as: Phys. Fluids **34**, 111902 (2022); https://doi.org/10.1063/5.0113826
Submitted: 24 July 2022 • Accepted: 29 September 2022 • Published Online: 02 November 2022

Yu Pan (潘宇) and Haibo Dong (董海波)

Physics of Fluids ARTICLE scitation.org/journal/phf

Effects of phase difference on hydrodynamic interactions and wake patterns in high-density fish schools

Cite as: Phys. Fluids **34**, 111902 (2022); doi: 10.1063/5.0113826
Submitted: 24 July 2022 · Accepted: 29 September 2022 ·
Published Online: 2 November 2022

View Online Export Citation CrossMark

Yu Pan (潘宇), and Haibo Dong (董海波)[a)]

AFFILIATIONS

Department of Mechanical and Aerospace Engineering, University of Virginia, Charlottesville, Virginia 22904, USA

[a)]Author to whom correspondence should be addressed: hd6q@virginia.edu

ABSTRACT

In this study, we numerically investigate the effects of the tail-beat phase differences between the trailing fish and its neighboring fish on the hydrodynamic performance and wake dynamics in a two-dimensional high-density school. Foils undulating with a wavy-like motion are employed to mimic swimming fish. The phase difference varies from 0° to 360°. A sharp-interface immersed boundary method is used to simulate flows over the fish-like bodies and provide quantitative analysis of the hydrodynamic performance and wakes of the school. It is found that the highest net thrust and swimming efficiency can be reached at the same time in the fish school with a phase difference of 180°. In particular, when the phase difference is 90°, the trailing fish achieves the highest efficiency, 58% enhancement compared with a single fish, while it has the highest thrust production, increased by 108% over a single fish, at a phase difference of 0°. The performance and flow visualization results suggest that the phase of the trailing fish in the dense school can be controlled to improve thrust and propulsive efficiency, and these improvements occur through the hydrodynamic interactions with the vortices shed by the neighboring fish and the channel formed by the side fish. In addition, the investigation of the phase difference effects on the wake dynamics of schools performed in this work represents the first study in which the wake patterns for systems consisting of multiple undulating bodies are categorized. In particular, a reversed Bénard–von Kármán vortex wake is generated by the trailing fish in the school with a phase difference of 90°, while a Bénard–von Kármán vortex wake is produced when the phase difference is 0°. Results have revealed that the wake patterns are critical to predicting the hydrodynamic performance of a fish school and are highly dependent on the phase difference.

I. INTRODUCTION

As a typical collective system and social aggregation, fish schools have long been hypothesized to provide hydrodynamic benefits to individuals through flow-mediated interactions.[1–4] Studies have suggested that the fish swimming in a school achieves improved propulsive performance by harvesting energy from vortex wakes,[5,6] enhancing thrust production,[1,7,8] or by reducing drag.[1,9] Our previous work has demonstrated that high-density schools significantly improve the hydrodynamic performance of swimmers through the wall effect and the block effect.[10] In addition to the spatial arrangement, phase differences are thought to be a significant factor in determining the extent of the performance improvement for the swimmers in a school.[7,11–13] However, the means whereby the phase difference influences the performance of individuals in high-density schools have seldom been reported, and the associated mechanisms remain obscure.

Biological experiments demonstrated that fish can alternate their tail-beat phase to capture energy from the vortex flow through the vortex–body interaction.[5,6] To further elucidate the interaction, some computational[14,15] and experimental studies[7,16] have been performed by using two in-line pitching foils. It is found that the performance of the trailing foil strongly depends on the phase difference between the leading and trailing foils because the phase difference affects the timing when the vortices shed by the leading foil arrive at the leading edge (LE) of the trailing foil and influence the formation of the leading-edge vortex (LEV).[14,15] For instance, Boschitsch *et al.*[7] reported that the thrust and the propulsive efficiency of the trailing foil could be enhanced by 60% more than that of an isolated foil when the phase difference is about 300° in the experiment of two in-line pitching foils at a spacing of 0.25 times the chord length.[7] Similar results were obtained in three-dimensional experiments using in-line foils conducted by Kurt and Moored.[16] Furthermore, flow visualizations reveal that the relative orientation of the tailing foil influences the vortex evolution and its hydrodynamic performance after the shedding vortices reach the leading edge of the trailing foil.[7] However, the means

whereby the vortex–body interaction affect the distributions of surface pressure and power consumption on a foil have barely been mentioned. Also, due to limiting to the oscillating rigid foil, how a fish, an undulating body, captures energy from the vortex flow has not been fully addressed.

Massive research has found that the wake interactions determine the hydrodynamic performance of swimmers in a side-by-side configuration and are dependent on the tail-beat phase difference.[11,12,17,18] Dewey *et al.*[11] performed experiments on a pair of pitching foils in a side-by-side configuration and reported that the swimming power is reduced in the in-phase case and thrust enhancement occurs in the anti-phase case, which results from the associated interaction of vortex pairs produced by the foils. Similar results were obtained in the two-dimensional numerical simulations using undulating foils.[12] In addition, the effects of phase difference on the hydrodynamic interactions in staggered schools, a more common configuration in nature, have received some limited attention.[13,19] Li *et al.*[13] measured the energy consumption of two bio-inspired fish-like robots swimming in a staggered configuration and suggested that when the tailbeat phase difference between the leader and the follower varies linearly with the streamwise distance, the follower can always obtain hydrodynamic benefits. However, the body–body interaction, occurring in the near flow field of the swimmers, which directly influences hydrodynamic performance, has not received significant attention in previous research.

Although the above-mentioned studies have significantly improved our understanding of the hydrodynamic interactions in fish schools, the schools are minimal, with only two swimmers, and have limited forms of hydrodynamic interactions. More recently, the hydrodynamic performance of fish schools containing more individuals has been investigated[10,20–28] using self-propelled particles[23,24,27] and numerical simulations based on the Navier–Stokes equations.[10,20,21,25,28] The hydrodynamic performance of schools with complex arrangements, including diamond-shaped[20] and rectangular configurations,[20,21] has been numerically studied in two[20] and three dimensions[21] by applying periodic boundary conditions. The results of these studies confirmed that individuals swim more efficiently in a school than when solitary.[20] Nevertheless, the phase difference effects were not considered, and quantitative analyses of the interactions were not presented due to the limitations of the numerical methods.

In this study, we numerically investigate the effects of tailbeat phase differences on hydrodynamic interactions in a high-density diamond-shaped school using an in-house incompressible Navier–Stokes solver based on the immersed boundary method. The phase difference varies from 0° to 360° by adjusting the phase of the trailing fish. A comprehensive quantitative analysis of hydrodynamic performance and flow fields then explores the hydrodynamic interactions in these schools. Also, the wake patterns of multiple undulating swimmers are categorized, and the phase difference effect on the wake dynamics is examined. The remainder of this paper is organized as follows: Section II describes the fish-like kinematics, the diamond-shaped school arrangement, numerical methods, simulation setup, and performance parameters. The numerical results, including the hydrodynamic performance of a single fish and individuals in different schools, are presented in Sec. III. The vortex capture mechanism, matching mechanism, and wake patterns are discussed in Sec. IV. Finally, the conclusions to this study are presented in Sec. V.

II. METHODS

A. Problem definition

The traveling wave kinematics are imposed on a NACA0012 foil to resemble two-dimensional carangiform fish-like swimming. The body length of the fish model is scaled to $L = 1$. The lateral displacement y of a point located at x on the fish body at time t is given by

$$y(x,t) = A(x) \cdot \sin\left(\frac{2\pi}{\lambda}x - \frac{2\pi}{T}t + \varphi\right), \tag{1}$$

$$A(x) = a_2x^2 + a_1x + a_0, \tag{2}$$

where $A(x)$ represents the amplitude of undulating motion at x, λ is the wavelength of the traveling wave over the body and fixed at $1.0L$, and T and φ denote the period and phase of the undulating motion, respectively. In Eq. (2), to mimic the carangiform motion, the coefficients are set to $a_0 = 0.02$, $a_1 = -0.08$, and $a_2 = 0.16$. More details about the fish model and the locomotion can be found in Ref. 10. Figure 1(a) shows the amplitude envelope $A(x)$ of the carangiform motion (red dashed lines) and the resulting sequenced midlines in a tail-beat period (blue lines).

To ensure the problem complexity remains manageable, we vary the undulating phase of the trailing fish (fish 4) from 0° to 360°, at intervals of 30°, while keeping the phase of the other fish at zero, in a high-density school with a lateral spacing of $D = 0.4L$ and a streamwise spacing of $S = 0.4L$, as shown in Fig. 1(b). The phase difference of the school is thus defined as the difference between the phase of fish 4 (φ) and that of the other fish (0°), i.e., φ. In these schools, fish 4 starts the undulating motion from different positions, marked with different colors in Fig. 1(b), compared with the other fish because of the phase difference. Figure 1(c) presents the lateral motion of the tail-tip point of fish 4 at different phases.

B. Numerical methods and case setup

The governing equations of the flow past a fish school are the two-dimensional incompressible viscous Navier–Stokes equations, written in the indicial form as

$$\frac{\partial u_i}{\partial x_i} = 0, \quad \frac{\partial u_i}{\partial t} + \frac{\partial u_i u_j}{\partial x_j} = -\frac{\partial p}{\partial x_i} + \frac{1}{Re}\frac{\partial^2 u_i}{\partial x_i \partial x_j}, \tag{3}$$

where u_i denotes the velocity components, p is the pressure, and Re is the Reynolds number.

The incompressible flow is solved using a finite-difference-based immersed boundary method.[29] Specifically, the equations are discretized in space using a cell-centered, collocated arrangement of the primitive variables and integrated in time using a fractional step method. The flow is simulated on non-conformal Cartesian grids, and boundary conditions are precisely imposed on the immersed boundary through a multi-dimensional ghost-cell technique. This method has been successfully applied in many simulations of biological flapping propulsions.[10,28,30,31] More details about this method and validation cases are provided in Ref. 29.

Figure 2(a) presents a schematic of the non-uniform Cartesian computational grids employed in the simulations, with a domain size of $12L \times 8L$. There are approximately 1.03×10^6 (1601×641) grid points in total, with a minimum grid spacing of $\Delta_{min} = 2.94 \times 10^{-3}$ L. The fish swim in the negative x-direction, and an incoming flow with

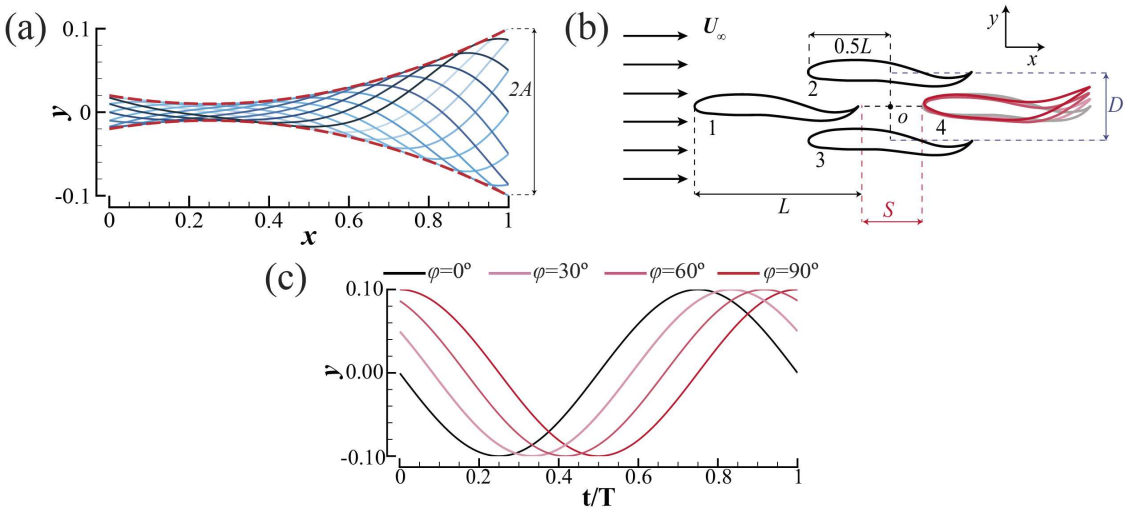

FIG. 1. (a) Amplitude envelopes of a carangiform motion (red dashed lines) and the sequenced midlines of the fish-body during one tail-beat period (blue lines). *A* is the lateral motion amplitude at the tail-tip. (b) Schematic of high-density diamond-like fish school with varied phase differences. Fish 4 in different schools is indicated by different colors. (c) Tail-tip motion of fish 4 with varied undulation phases.

a constant velocity of U_∞ is applied as the boundary condition at the left-hand boundary. The right-hand boundary is assigned the outflow boundary condition, and the zero-gradient boundary condition is employed at lateral boundaries. As for the pressure, a homogeneous Neumann boundary condition is imposed on all boundaries.

A grid-independence study was conducted to prove that the current grid setup is fine enough to obtain accurate results. Figure 2(b) compares the instantaneous net force coefficient C_X (along the swimming direction) of a solitary fish calculated using coarse, medium, fine, and dense meshes. As the grid spacing decreases, C_X converges. The percentage difference between the peak values of the fine grid and the dense grid is less than 2%. Therefore, the fine grid is employed for all simulations described below.

Two dimensionless parameters, the Reynolds number *Re* and the Strouhal number *St*, are defined to examine the hydrodynamics and flow characteristics of fish-like swimming. $Re = U_\infty L/\upsilon$, where ν denotes the kinematic viscosity; $St = 2fA/U_\infty$, where $f = 1.0$ represents the tail-beat frequency and $A = 0.1$ is the lateral motion amplitude at the tail-tip. Following previous work,[10] the Reynolds number and the Strouhal number are set to $Re = 1000$ and $St = 0.43$, which satisfy the steady swimming condition. Thus, the incoming flow velocity is set as $U_\infty = 0.465$.

In the solver, the hydrodynamic force F_X is calculated by integrating the projected surface pressure and shear force over the surface of a fish body. For convenience, we set F_X along the swimming direction, i.e., $F_X > 0$ denotes that it points to the swimming direction and is a net thrust. Thus, the F_X can be expressed as

$$F_X = -\int_S (-pn_x + \tau_{xi}n_i)dS, \tag{4}$$

where the indices $i = x, y$ represent the *x*- and *y*-direction, respectively, and τ_{ij} denotes the viscous stress tensor and n_i is the *i*th

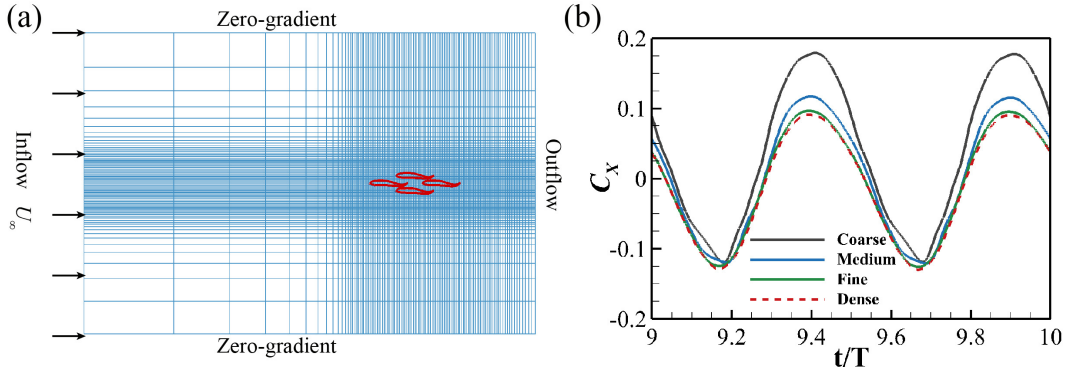

FIG. 2. (a) Schematic of the computational mesh and boundary conditions employed in this study, where U_∞ is the incoming flow velocity. The fish school is marked in red. (b) Grid independence study on C_X for a solitary fish with a coarse mesh ($\Delta_{min} = 0.011L$), medium mesh ($\Delta_{min} = 5.88 \times 10^{-3}$ L), fine mesh ($\Delta_{min} = 2.94 \times 10^{-3}$ L), and dense mesh ($\Delta_{min} = 1.92 \times 10^{-3}$ L).

component of the unit normal vector of any element dS on the fish body. For an undulating body, F_X is the summation of the thrust F_T and the drag F_D, $F_X = F_T + F_D$. The thrust F_T is computed by integrating according to the pressure and viscous stress signs and can be expressed as follows:

$$F_T = \frac{1}{2}\left(-\int_S -pn_x dS + \left|\int_S pn_x dS\right|\right) + \frac{1}{2}\left(-\int_S \tau_{xi} n_i dS + \left|\int_S \tau_{xi} n_i dS\right|\right). \quad (5)$$

More details about the calculation of the forces can be found in Ref. 10.

The forces are normalized as the coefficients of net x-force (C_X), thrust (C_T), and drag (C_D) and can be expressed as $C_i = F_i/0.5\rho U_\infty^2 L$, where i denotes the different forces defined above. The output power required to deform the body is defined as $P_U = \oint -(\bar{\bar{\boldsymbol{\sigma}}} \cdot \boldsymbol{n}) \cdot \boldsymbol{u}\, dS$, where $\bar{\bar{\boldsymbol{\sigma}}}$ denotes the stress tensor, $\boldsymbol{n}$ is the normal vector of an element dS, and $\boldsymbol{u}$ is the relative velocity to the incoming flow, i.e., the deformational velocity of the element.[32,33] Similarly, the dimensionless power coefficient C_{PW} is computed as $C_{PW} = P_U/0.5\rho U_\infty^3 L$. Unlike oscillating swimming, the definition of propulsion efficiency in undulating swimming has been long debated,[33–35] especially for the steady swimming condition. Following previous work,[10] we employ the modified Froude efficiency η to measure the propulsive efficiency of undulating swimming,

$$\eta = \frac{\overline{P_T}}{\overline{P_T} + \overline{P_U}} = \frac{\overline{F_T} U_\infty}{\overline{F_T} U_\infty + \overline{P_U}} = \frac{\overline{C_T}}{\overline{C_T} + \overline{C_{PW}}}, \quad (6)$$

where overlines denote cycle-averaged values and $\overline{P_T}$ represents the average power output related to thrust production.

III. RESULTS

A. Performance of a single fish in steady swimming

In a previous study, we examined the hydrodynamic performance, vortex wake, and time-averaged velocity field of a single fish in steady swimming.[10] Here, a more comprehensive analysis of the hydrodynamic performance of a single fish is performed by identifying the spatiotemporal distribution of the force generation in the x-direction and power consumption required for deformation during one cycle (see Fig. 3). In each panel of Fig. 3, the x-axis indicates the position along the body and the y-axis denotes the time in one period. Blue represents suffering drag or the capture of energy from vortex flow, and red indicates the production of thrust or consumption of power.

The force generation and power consumption patterns of a solitary 2D swimmer, shown in Figs. 3(a) and 3(b), are similar to those of a three-dimensional mackerel,[36] which is also a carangiform swimmer. Unsurprisingly, the fish snout always suffers drag, while the tail generates most of the thrust, as shown in Fig. 3(a). The high-thrust-production region extends from roughly 0.65 to 0.95L on the body, and two thrust peaks appear near 0.82L. Due to the smaller undulation amplitude, the force at the middle part of the body is close to zero.

The power consumption shows a similar traveling wave pattern as the force generation, whereas the high-power-consumption regions are longer and narrower than the high-thrust regions. Two large areas of negative power consumption appear on the posterior part of the body. Negative power consumption indicates that the body extracts energy from the fluid environment, which implies a potential to improve propulsive efficiency.

B. Hydrodynamic performance of individuals in a school

Due to the strong body–body interaction in the high-density diamond-shaped school, the performance of individuals can be significantly influenced by the phase difference. Figure 4 presents the time-averaged hydrodynamic performance of individuals in schools varying with the phase difference. A school's performance is calculated by averaging that of the four swimmers; the results are also shown in Fig. 4. Due to symmetry, fish 3 has the same propulsive performance as fish 2 and the results shown for fish 2 are representative of both fish 2 and fish 3.

Figure 4(a) shows the relationship between the time-averaged net force in the x-direction $\overline{C_X}$ and the phase difference. First, for all the fish in these schools, $\overline{C_X}$ is greater than zero and is a net thrust. This implies that fish in a high-density school can always gain a net thrust, regardless of position or phase difference. Both $\overline{C_X^1}$ and $\overline{C_X^4}$ are more sensitive to the phase variation than $\overline{C_X^2}$. (Here, the superscript denotes different fish in a school.) $\overline{C_X^1}$ exhibits an approximate cosinusoidal shape, while $\overline{C_X^4}$ displays the opposite trend as φ increases. $\overline{C_X^2}$ has a bell shape and is symmetric about the $\varphi = 180°$. Remarkably, fish 4 obtains the highest net thrust in the school in most situations. When

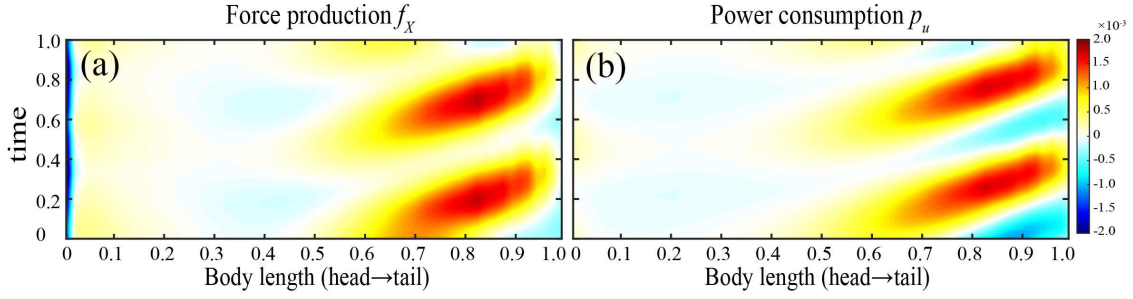

FIG. 3. Spatiotemporal distribution of (a) force production in the x-direction $f_X = -(-pn_x + \tau_{xi}n_i)$ and (b) power consumption for undulating motion $p_u = -(\bar{\bar{\boldsymbol{\sigma}}} \cdot \boldsymbol{n}) \cdot \boldsymbol{u}$ along the fish body during one period. Positive values, marked in red, denote thrust [in (a)] or output power [in (b)], while negative values indicate drag [in (a)] or input power [in (b)].

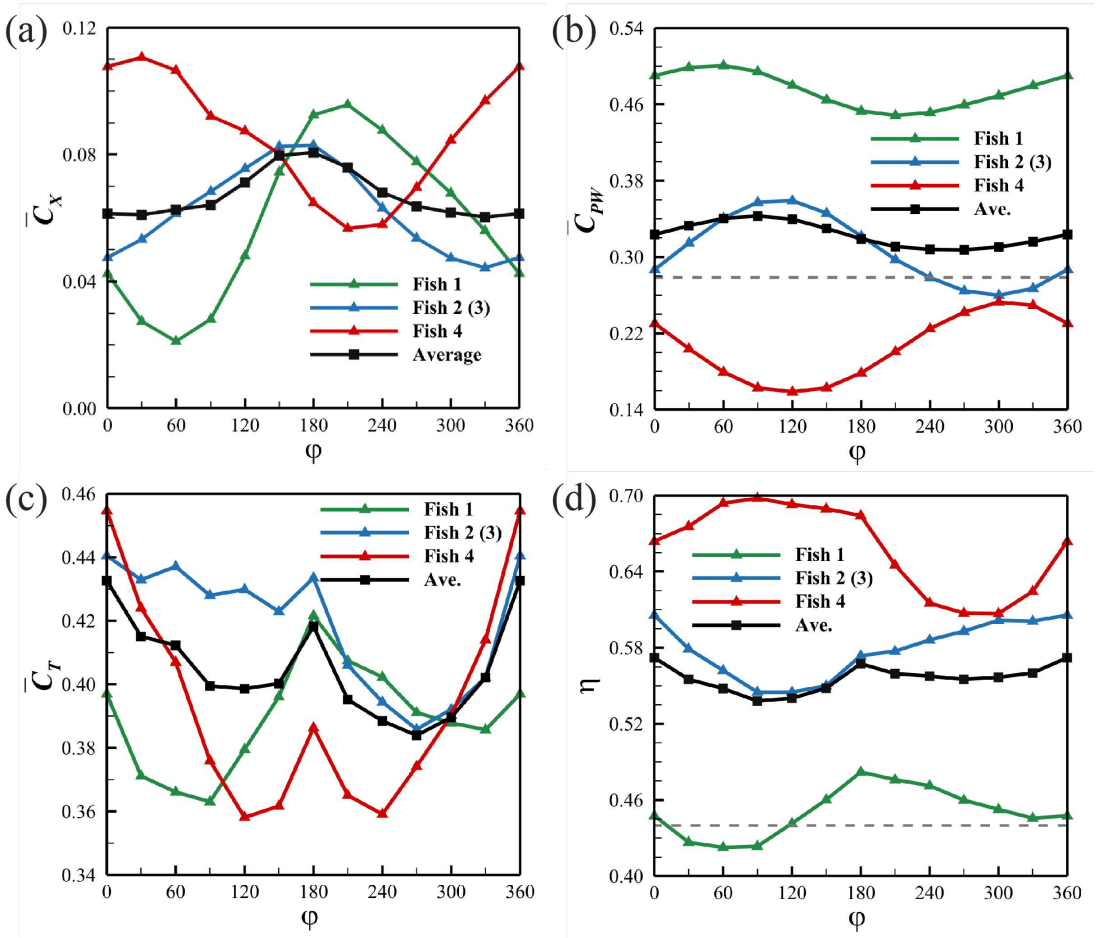

FIG. 4. Hydrodynamic performance of each fish as a function of phase difference φ in high-density fish schools: (a) time-averaged net force coefficient in the *x*-direction $\overline{C_X}$, (b) time-averaged power consumption coefficient $\overline{C_{PW}}$, (c) time-averaged total thrust coefficient $\overline{C_T}$, and (d) hydrodynamic efficiency η. The gray dashed lines in (b) and (d) denote $\overline{C_{PW}}$ and η for a solitary fish in steady swimming, respectively.

$\varphi = 30°$, $\overline{C_X^4}$ reaches its maximum value of $\overline{C_{X\,\max}^4} = 0.111$, 15.6% larger than $\overline{C_{X\,\max}^1} = 0.096$, and 33.7% higher than $\overline{C_{X\,\max}^2} = 0.083$. The minimum value of $\overline{C_X^4}$ is 0.057 at $\varphi = 210°$, and this value is larger than $\overline{C_{X\,\min}^1}$ and $\overline{C_{X\,\min}^2}$.

Figure 4(b) presents the time-averaged power consumption coefficient for undulating motion $\overline{C_{PW}}$ with respect to the phase difference. The gray dashed line denotes $\overline{C_{PW}}$ for a solitary fish, $\overline{C_{PW}^s} = 0.278$. $\overline{C_{PW}^1}$, $\overline{C_{PW}^2}$, and $\overline{C_{PW}^{ave}}$ display sinusoidal waveforms, whereas $\overline{C_{PW}^4}$ exhibits the opposite trend. By comparison, fish 1 consumes the most energy in a school regardless of phase difference. This can be explained by the block effect.[10] At $\varphi = 60°$, $\overline{C_{PW}^1}$ reaches its maximum value of $\overline{C_{PW\,\max}^1} = 0.501$, which is 80.2% higher than that of a solitary fish. Surprisingly, fish 4 consumes less energy than a solitary fish and the other fish in the school at all phases. The maximum occurs at $\varphi = 300°$, where $\overline{C_{PW\,\max}^4} = 0.256$, which is less than $\overline{C_{PW}^s}$. At $\varphi = 120°$, $\overline{C_{PW}^4}$ reaches its minimum of 0.159, which is 42.8% less than $\overline{C_{PW}^s}$. The variation of $\overline{C_{PW}^4}$ implies that the trailing fish can save more energy by changing its phase in a high-density school.

Figure 4(c) displays the variation of the time-averaged total thrust coefficient $\overline{C_T}$ of each fish in the high-density schools. For a single fish, $\overline{C_T}$ is around 0.219.[10] First, from Fig. 4(c), it can be seen that $\overline{C_T}$ for each fish in the schools is much larger than that of a single fish ($\overline{C_T^s}$). $\overline{C_{T\,\max}^4}$ is 107.8% higher than $\overline{C_T^s}$ ($\overline{C_{T\,\max}^4} = 0.455$, which occurs at $\varphi = 0°$.), and $\overline{C_{T\,\min}^4}$ is 63.5% higher than $\overline{C_T^s}$ ($\overline{C_{T\,\min}^4} = 0.358$, which occurs at $\varphi = 120°$). The curves of $\overline{C_T}$ for each fish are approximately W-shaped, although they are somewhat different. Fish 2 and fish 4 attain their maximum values at $\varphi = 0°$ ($\overline{C_{T\,\max}^2} = 0.440$), while fish 1 gains its largest thrust of $\overline{C_{T\,\max}^1} = 0.422$ at $\varphi = 180°$. Compared with the other fish, $\overline{C_T^4}$ is more dependent on the phase difference. The difference between $\overline{C_{T\,\max}^4}$ and $\overline{C_{T\,\min}^4}$ is 0.097, 44.3% of $\overline{C_T^s}$, and is much larger than that of the other fish. According to the definitions of thrust and drag, we can obtain $\overline{C_D}$ by subtracting $\overline{C_X}$

from $\overline{C_T}$. The results show that, at any φ, the relationship among $\overline{C_D^1}$, $\overline{C_D^2}$, and $\overline{C_D^4}$ is that $\overline{C_D^4} < \overline{C_D^1} < \overline{C_D^2}$, which implies that fish 4 experiences the smallest drag in a high-density school.

Figure 4(d) plots the variation of the propulsive efficiency vs the phase difference. The gray dashed line denotes the swimming efficiency of a single fish ($\eta^s = 0.441$). First, there exists an approximately sinusoidal relationship between η^4 and the phase φ, while η^1 exhibits an opposite trend. η^2 and η^{ave} present W-shaped profiles. When $\varphi = 90°$, η^4 reaches its maximum of $\eta^4_{max} = 0.698$, which is 58.3% higher than that of a solitary fish. However, η^1, η^2, and η^{ave} reach their minimum at this phase difference: $\eta^1_{min} = 0.423$, $\eta^2_{min} = 0.545$, and $\eta^{ave}_{min} = 0.538$. It has been observed that fish 4 gains higher swimming efficiency than other fish in a school and a solitary fish, regardless of phase difference. In particular, the minimum η^4 ($\eta^4_{min} = 0.607$ at $\varphi = 270°$) is 37.6% higher than η^s and is also larger than $\eta^1_{max} = 0.482$ and $\eta^2_{max} = 0.605$.

Based on the above discussion, we conclude that the trailing fish, fish 4, can save the most energy for undulating motion, suffer the lowest drag and achieve the highest swimming efficiency by maintaining an appropriate phase difference in a high-density school. Two associated assumptions explain this: (1) the phase difference affects the interaction between the vortices shed by fish 2 and fish 3 and the undulating body of fish 4 and (2) the phase difference alters the flow environment around the anterior part of fish 4 in the channel formed by fish 2 and fish 3. The hydrodynamic performance of fish 4 is thoroughly investigated in Sec. IV.

IV. DISCUSSION

A. Performance of trailing fish in a dense fish school

To reveal the underlying mechanisms, four typical schools are considered: school 1 ($\varphi = 0°$), school 2 ($\varphi = 90°$), school 3 ($\varphi = 180°$), and school 4 ($\varphi = 270°$). Figure 5 presents the time history of the hydrodynamic performance of fish 4 in each school, including the total thrust coefficient C_T, power coefficient C_{PW}, and x-direction net force coefficient C_X. We denote the thrust coefficient of fish 4 in school I as C_{iT}. A similar definition is used for other coefficients. For comparison, the timelines of schools 2, 3, and 4 are shifted so that fish 4 has the same undulation motion in all four schools.

Figure 5 shows a more detailed influence of the phase difference on hydrodynamic interactions by presenting the time history of the performance of fish 4. First, the peaks of C_T, C_{PW}, and C_X are incredibly varied in different schools. The highest peak of C_T is $C_{1T\_peak} = 0.642$ at $t = 9.17T$ in school 1. This value is 42% higher than the peak in school 2 ($C_{2T\_peak} = 0.452$ at $t = 9.48T$). Correspondingly, fish 4 has the highest peak of C_{PW} in school 1 ($C_{1PW\_peak} = 0.469$ at $t = 9.78T$), and this is 31.7% higher than $C_{2PW\_peak} = 0.356$ at $t = 9.78T$, the lowest peak. For C_X, the highest peak still occurs in school 1 ($C_{1X\_peak} = 0.417$ at $t = 9.16T$), which is 113% higher than $C_{4X\_peak} = 0.196$ at $t = 9.20T$. In addition, the times of the peaks are shifted. For instance, in Fig. 5(a), the peaks of C_{1T} are at $t = 9.17$ and $t = 9.67T$, while the peaks of C_{2T} are at $t = 9.48$ and $t = 9.98T$, respectively. In addition, the C_T curves, except for school 1 ($\varphi = 0°$), present a higher level of fluctuation than the C_X and C_{PW} curves. It is because C_T implies more specific information about force generation along the swimming direction and is more sensitive to the flow variation, which can be derived from their definitions. The differences in performance suggest that the time and extent of constructive interactions for fish 4 can be dramatically altered by the flow environment which depends on the phase difference. This implies that the trailing fish can further improve thrust production and reduce power consumption by varying its phase.

To clearly show the phase difference effect on hydrodynamic interactions, Fig. 6 presents the spatiotemporal distribution of force generation and power consumption along the body of fish 4 during one cycle in these four schools. Dark red regions in Figs. 6(a)–6(d) indicate areas of high thrust produced by fish 4. By comparison, fish 4 generates much more thrust than a solitary fish at the tail. The anterior part of fish 4 produces high thrust during most of a cycle instead of only suffering drag [Fig. 3(a)]. However, when and how much thrust can be generated depend on the phase difference, both at the head and tail of fish 4. Compared with the rear part of fish 4 in school 1 [Fig. 6(a)], the corresponding high-thrust regions in school 2 [Fig. 6(b)] are stretched, but the strength decreases and the times of the centers are shifted upward. Additionally, the anterior part of fish 4 generates high thrust in school 2 from $t = 0$ to $t = 0.1T$ [Fig. 6(b)], whereas it suffers drag in school 3 [Fig. 6(c)]. Similar phenomena are found for the power consumption in Figs. 6(e)–6(h). Remarkably, when $\varphi = 90°$, the strength of the high-power regions becomes much

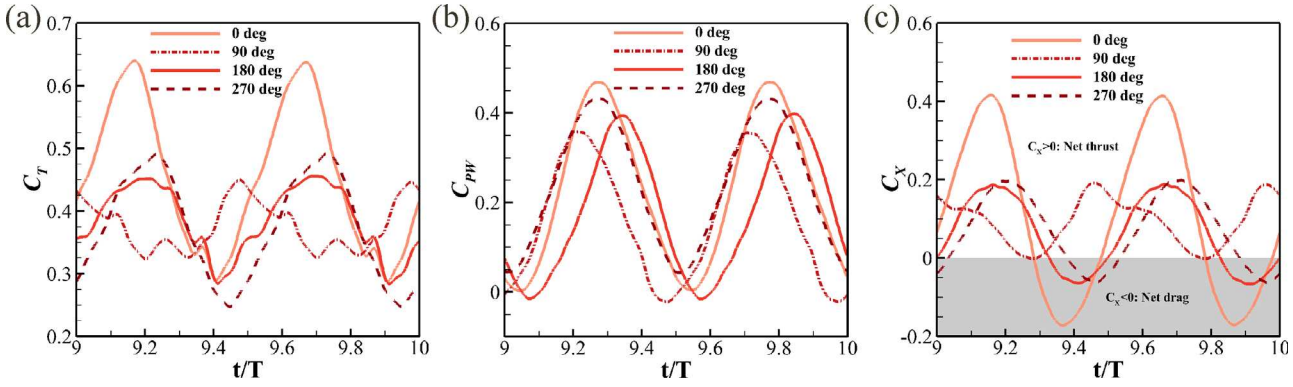

FIG. 5. Time history of hydrodynamic performance of fish 4 in the schools with $\varphi = 0°$, 90°, 180°, and 270°: (a) total thrust coefficient C_T, (b) power consumption coefficient C_{PW}, and (c) net force coefficient in the x-direction C_X.

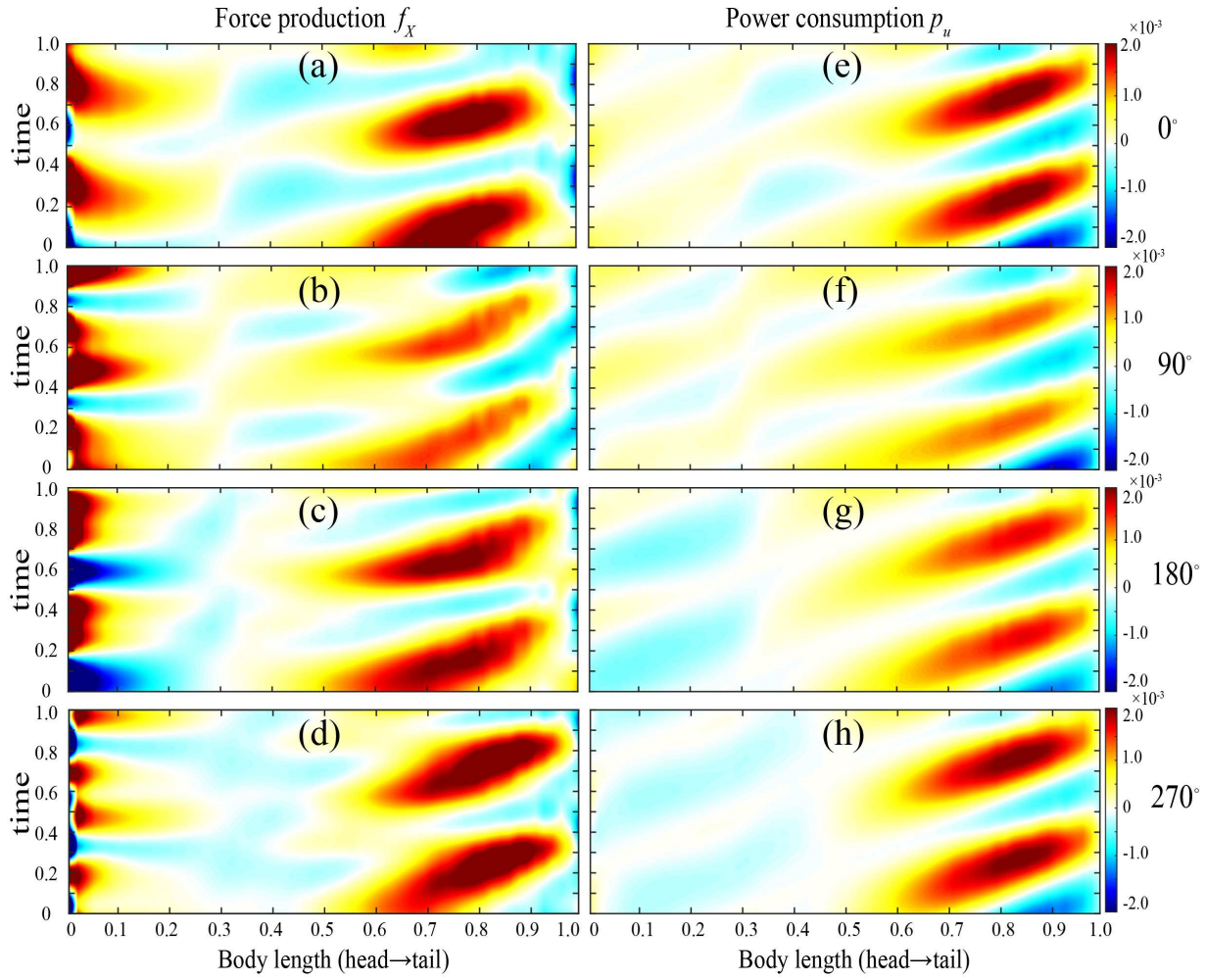

FIG. 6. Spatiotemporal distribution of force production f_x (a)–(d) and power consumption p_u (e)–(h) of fish 4 in four different schools. Positive values, marked in red, denote thrust or output power, while negative values indicate drag or input power.

weaker than in other schools, which implies that less energy is consumed by fish 4 for undulation in school 2. The blue regions in Fig. 6(f) suggest that fish 4 extracts energy from the flow. This results in the highest swimming efficiency of fish 4 occurring in school 2 ($\eta^4_{\max} = 0.698$). According to the force generation and power consumption patterns shown in Fig. 6, we can quickly determine, which part of the body affects the hydrodynamic performance and the extent to which the phase difference influences this.

Furthermore, to quantitatively clarify the performance variations, the body of fish 4 is evenly divided into ten segments, and the hydrodynamic performance of each segment is calculated separately and illustrated. Figure 7 shows the flow-induced force vectors on the body of fish 4, the thrust production and power consumption of each segment of fish 4 in the two schools, school 1 and school 2, at two times, $t = 0.25$ and $t = 0.50T$. Based on the position of fish 4 in the high-density schools, it can be divided into two essential parts: (1) the anterior part, 0–0.3L, located in the channel formed by fish 2 and fish 3, (2) the posterior part, 0.3–1.0L, out of the channel. The phase difference effects on these two parts can be separately and quantitively investigated. First, when $t = 0.25T$, the anterior part of fish 4 generates high thrust ($C^a_{1X} = 0.079$) in school 1 [see Fig. 7(a2)], and consumes power of $C^a_{1PW} = 0.012$ for undulating motion [see Fig. 7(a3)], while in school 2, it suffers drag ($C^a_{2X} = -0.051$) [Fig. 7(b2)], and captures energy from the flow ($C^a_{2PW} < 0$) [Fig. 7(b3)]. For the posterior part, at $t = 0.50T$, fish 4 generates a large thrust ($C^p_{1X} = 0.157$) in school 1 with a small power consumption of $C^p_{1PW} = 0.002$. For comparison, fish 4 produces a much lower thrust ($C^p_{2X} = 0.094$) in school 2 and consumes much more power ($C^p_{4PW} = 0.014$) in school 4.

The differences in performance shown in Figs. 6 and 7 suggest the mutual interaction between the vortical flow and the posterior part (vortex–body interaction) and the interaction between the anterior part and the channel (body–body interaction) affect the hydrodynamic performance of fish 4 as the phase difference varies. Based on these findings, the fundamental flow physics of the phase difference effects in a high-density school are discussed in Secs. IV B and IV C.

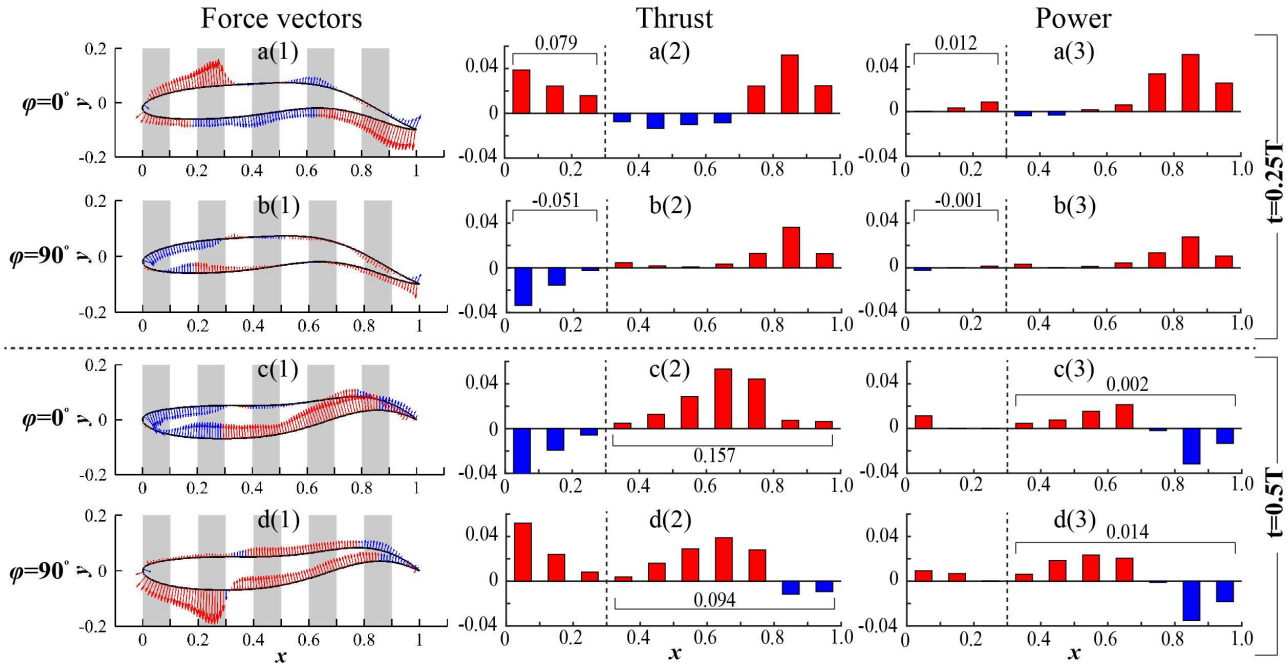

FIG. 7. Force vectors along fish 4 (a1)–(d1), thrust production (a2)–(d2), and power consumption for undulation (a3)–(d3) of each segment on fish 4 in the two schools, $\varphi = 0°$ and $\varphi = 90°$, at $t = 0.25$ and $t = 0.5T$. Blue denotes drag or capturing energy, and red represents generating thrust or exhausting energy.

B. Vortex capture mechanism between neighboring fish

The flow fields of schools 1 and 2 are now analyzed and compared to explore the phase difference effects on the vortex-undulating body interaction. Figure 8 presents the undulating velocity along fish 4, the vortex wake and the pressure field around fish 4 in schools 1 and 2 at $t = 0.25$ and $0.75T$. Because of the symmetry of the schools, only the interaction between the shedding vortices of fish 2 and the upper surface of fish 4 is analyzed. To quantify the variation in the interactions, we display the hydrodynamic performance of the upper surface of fish 4 in schools 1 and 2 at $t = 0.25$ and $0.75T$ in Fig. 9.

In these high-density schools, vortex pairs are formed due to the wall effect[10] and shed downstream at different positions with respect to fish 4 at a specific time. When $t = 0.25T$, the vortex pair $V_{11}V_{12}$ is located at around $x = 9.5$ in school 1, as shown in Fig. 8(a2), whereas the vortex pair $V'_{11}V'_{12}$ is located at $x = 9.7$ in school 2 [Fig. 8(c2)]. This difference results in the pressure field around the upper surface of fish 4 changing from negative-dominant [in school 1, Fig. 8(a3)] to positive-dominant [in school 2, Fig. 8(c3)]. Considering the undulating motion of fish 4 at $t = 0.25T$, it can be deduced that fish 4 produces higher thrust but consumes more power, in school 2 than in school 1, which is verified by the quantitative results in Figs. 9(a1)–9(a2) and 9(c1)–9(c2). Similar phenomena can be observed at other times. For instance, when $t = 0.75T$, the difference in the positions of the vortex pair $V_{11}V_{12}$ [around $x = 9.8$, Fig. 8(b2)] and $V'_{11}V'_{12}$ [around $x = 10.0$, Fig. 8(d2)] leads to that the pressure magnitude around the tail of fish 4 is much larger in school 1 than in school 2. Thus, a higher suction thrust is generated in school 1, corresponding to more energy consumed by the upper surface to overcome the higher suction force. The quantitative differences are shown in Figs. 9(b1)–9(b2) and 9(d1)–9(d2).

In Figs. 8(a2) and 8(b2), it can be observed that a secondary vortex iV_1 is induced and advected downstream along the undulating body. The induced secondary vortex attaches to the upper surface of fish 4, and its rotation direction is opposite to that of the vortex attached to the boundary. However, in Figs. 8(c2) and 8(d2), the induced secondary vortex iV'_1 decays rapidly and does not move downstream. Thus, the secondary vortex is induced at the anterior part of fish 4 regardless of phase difference, but whether it becomes fully developed and moves downstream depends on the phase difference.

Additionally, the induced vortex moving along the body can modify the local pressure on the body to be negative or augment the magnitude of the negative pressure. The local curvature and the lateral motion should also be considered to determine whether the induced vortex is beneficial or detrimental to hydrodynamic performance. When $t = 0.25T$, the induced vortex iV_1 is located at $x = 9.5$–9.7 in school 1 [Fig. 8(a2)], and the local pressure on this part becomes negative [Fig. 8(a3)], unlike in school 2 [Fig. 8(c3)]. Considering the local curvature and the lateral motion [Fig. 8(a1)], it can be deduced that drag is produced and energy is captured from the flow by the associated part of the body. The quantitative results are shown in Figs. 9(a1) and 9(a2). In addition, when $t = 0.75T$, the induced vortex iV_1 moves to $x = 9.8$–$1.0L$ [see Fig. 8(b2)], and the amplitude of the pressure increases at the corresponding location in school 1. Therefore, much more thrust is generated, and more power is consumed by the upper surface of fish 4 in school 1, as shown in Figs. 9(b1) and 9(b2).

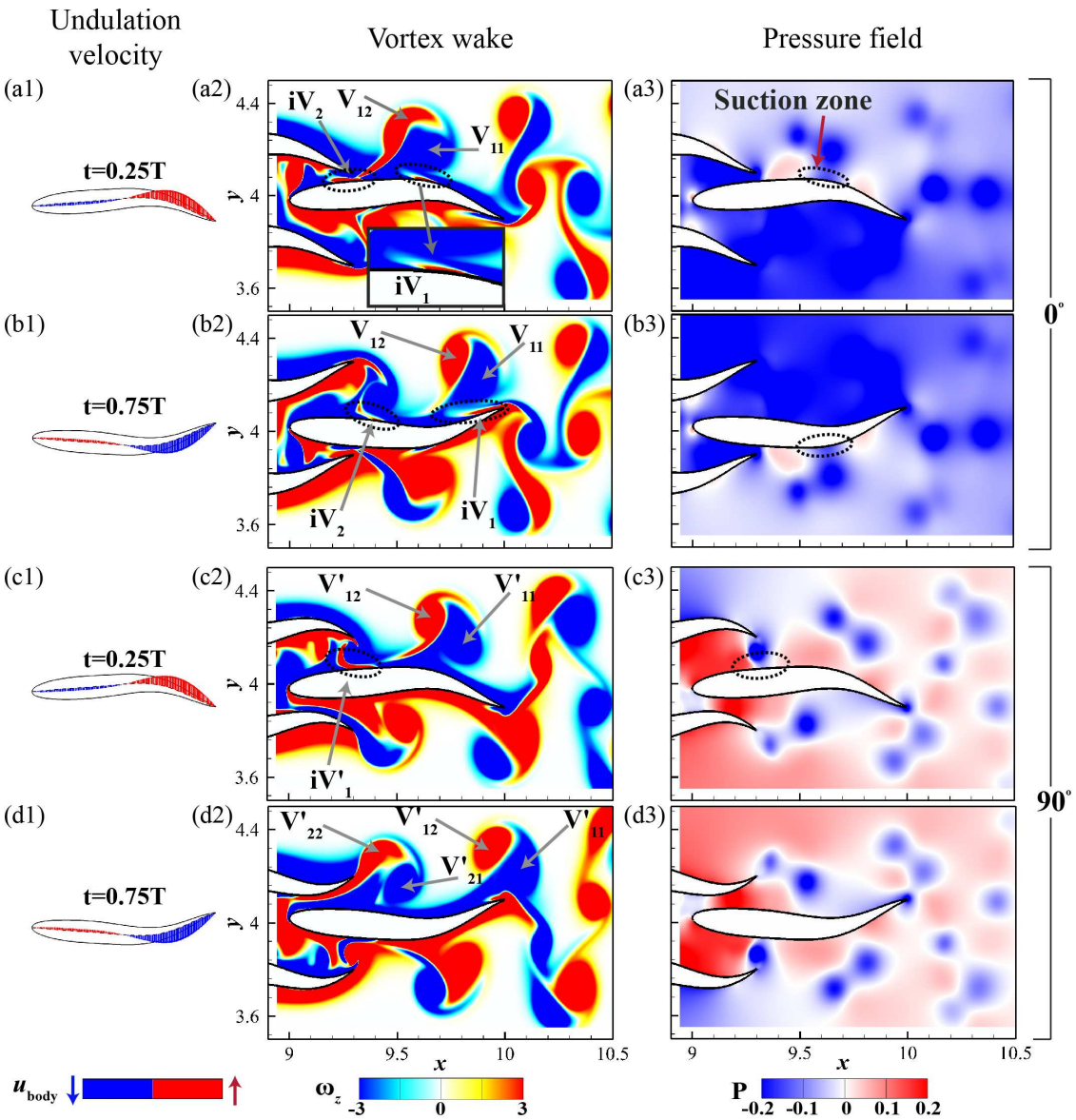

FIG. 8. Undulation velocity along fish 4 (a1)–(d1), vortex wake (a2)–(d2), and pressure field (a3)–(d3) around fish 4 in schools 1 and 2 at $t = 0.25$ and $0.75T$.

Two aspects of the vortex capture mechanism for an undulating swimmer have been revealed: (1) the interaction between vortex pairs and the undulating body and (2) the induction and convection of a secondary vortex. To concisely illustrate the two mechanisms, the associated schematics are displayed in Fig. 10. Figure 10(a) defines the location o, advection velocity u_p and rotation angle β for a vortex pair. The location of a vortex pair is defined as the midpoint of the cores of the two vortices, and the vortex cores are located at the local extremum of vortices;[37] for the definitions of the advection velocity and rotation angle, see Refs. 37 and 10, respectively. Figures 10(b) and 10(c) are based on the plots in Figs. 8(b2) and 8(d2), respectively, showing the vortex field around the upper surface of fish 4 in schools with various phases. First, in Figs. 10(b) and 10(c), the vortex pairs are at different locations because of the phase difference, influencing the interaction between the vortex pair and fish 4. These figures suggest that the trailing fish can achieve the optimal hydrodynamic performance in a high-density school by adjusting the phase. The mechanism also explains how trout save energy in the vortex wake of a D-section cylinder.[5] Second, there is a secondary vortex (iV_1), the red vortex attached to the body surface in Fig. 10(b), transported downstream; however, this is not observed in the other school [Fig. 10(c)]. The attached vortex alters the surrounding pressure, which dramatically influences the

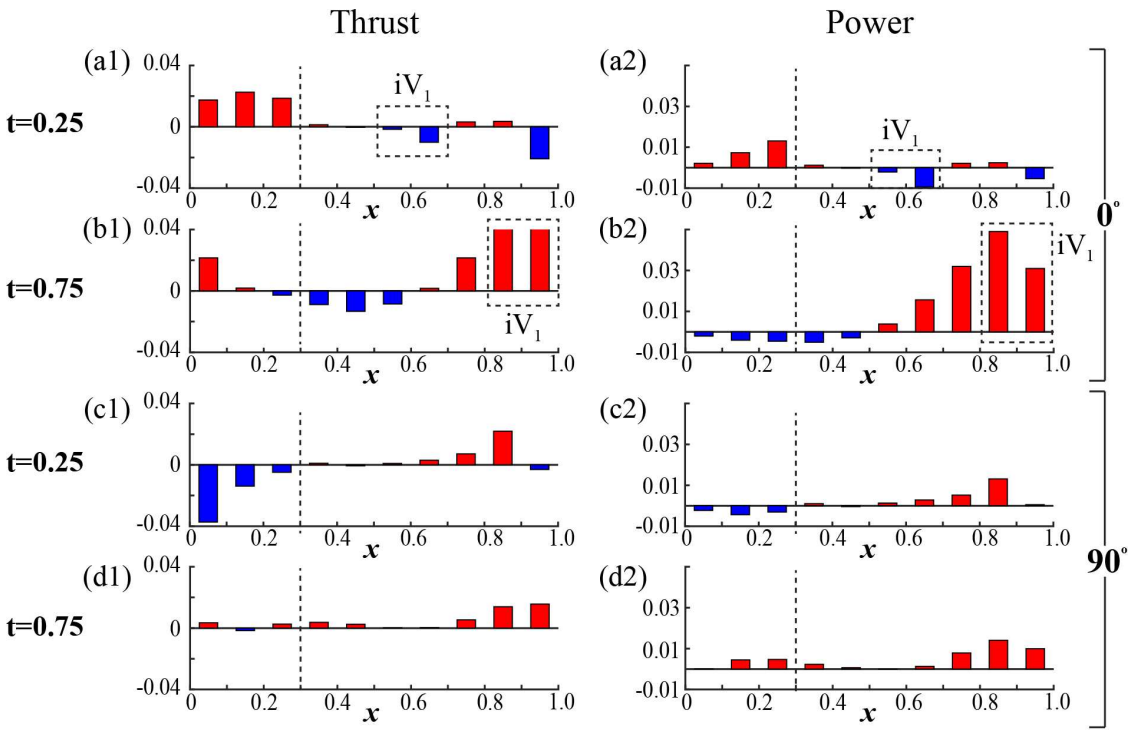

FIG. 9. Thrust (a1)–(d1) and power consumption for undulation motion (a2)–(d2) of each segment on the upper surface of fish 4 in schools 1 and 2 at $t = 0.25$ and $0.75T$.

thrust production and power consumption at the corresponding position on the body. The advection of the secondary vortex depends on the phase difference. From our observations, when $0° \leq \varphi < 90°$ or $270° < \varphi \leq 360°$, the secondary vortex can be advected downstream. Moreover, the secondary induced vortex is viscosity-dominated.[38] These results imply that the viscous effect should not be neglected when studying hydrodynamic interactions in a high-density fish school. A similar conclusion was mentioned in a previous study on three-dimensional fish swimming.[25]

C. Suction thrust and the body–body matching mechanism

In Fig. 3(a), the anterior part (0.0–0.3L) of a single fish mainly generates drag, while in Figs. 6(a)–6(d), the same part of fish 4 produces thrust in a high-density school. It can also be observed that the magnitude of the force generation and power consumption of the anterior part of fish 4 depend strongly on the phase difference of the fish school. For instance, compared with the thrust region at the anterior part of fish 4 in school 4, the corresponding thrust region is much larger in school 1. Next, we compare the performance of the anterior part of fish 4 in schools 1 and 4 to measure the phase difference effect.

Figure 11 shows the time history of the net force coefficient C_X^a and power consumption coefficient C_{PW}^a for the anterior part of fish 4 in schools 1 and 4. The superscript a denotes the anterior part. First, $\overline{C_{1X}^a} = 0.048$ and $\overline{C_{4X}^a} = 0.023$, implying a net thrust generated at the anterior part of fish 4 in both schools during one tail-beat cycle. In Fig. 11(a), compared with C_{1X}^a, the peaks and troughs of C_{4X}^a have shifted to the left by $0.25T$, which indicates the flow environment around the anterior part, determined by the phase difference, controls the force generation. Second, in Fig. 11(b), $C_{1PW}^a > 0$ and $C_{4PW}^a < 0$ during the

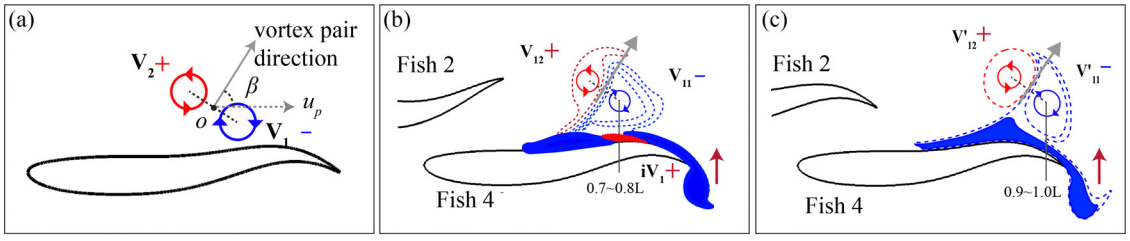

FIG. 10. (a) Definitions of the location o, advection velocity u_p, and rotation angle β for a vortex pair, (b) schematic of vortex–body interaction in school 1, and (c) schematic of vortex–body interaction in school 2.

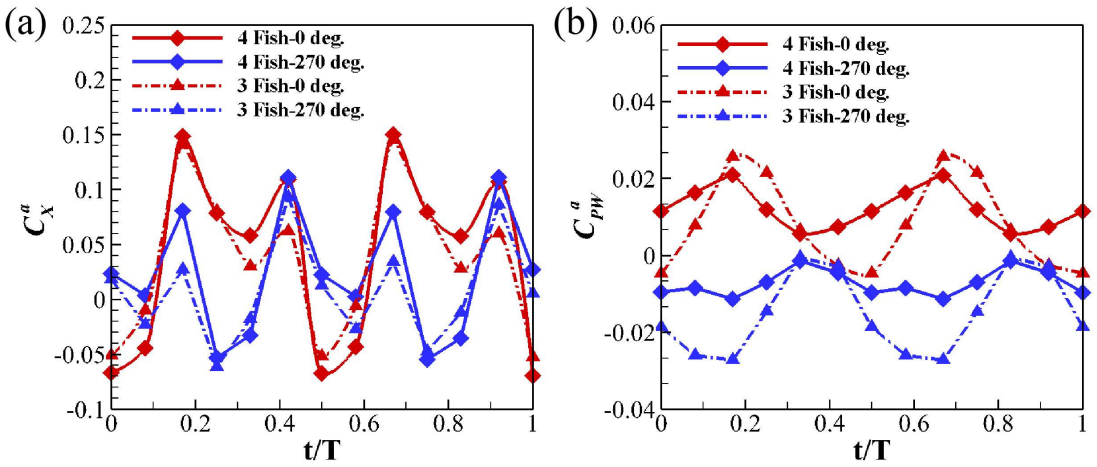

FIG. 11. Time history of (a) net force coefficient in the *x*-direction C_X^a and (b) power consumption coefficient C_{PW}^a of the anterior part of fish 4 in schools 1 and 4.

whole cycle. This suggests that the anterior part of fish 4 consumes power in school 1, while it extracts energy from the flow in school 4.

The anterior part of fish 4 can improve its performance by generating more thrust or capturing energy from the flow in a high-density school. However, the extent to which the improvement can be achieved depends on the phase difference. The phase difference effect stems from two aspects: (1) the interaction between shedding vortices of fish 1 and the anterior part of fish 4, and (2) the body–body interactions between the channel formed by fish 2 and fish 3 and the anterior part of fish 4. First, due to the phase difference, the vortices shed by fish 1 may impinge on the anterior part of fish 4 at different locations. Second, the body–body interaction between the undulating channel and the anterior part of fish 4, controlled by the phase difference, may change the flow rate of the channel, which, in turn, modifies the flow environment around the anterior part.

The vortex–body interaction has been studied by many researchers.[7,8,28,39,40] In contrast, the body–body interaction between an undulating channel and a fish body is unique to high-density diamond-shaped schools and has not yet been reported. To measure the influences of these two aspects, we remove the leading fish, fish 1, and simulate the hydrodynamics of triangular fish schools at $\varphi = 0°$ and $\varphi = 270°$. The hydrodynamic performance of the anterior part of the trailing fish in triangular schools is also presented in Fig. 11. The variation of C_X^a is large when the phase changes, for both diamond-shaped and triangular fish schools, whereas it is very small between the two kinds of schools with the same phase, as shown in Fig. 11(a). This suggests that the matching between the channel and fish 4 plays a dominant role in force generation, while the vortex–body interaction is less important. Additionally, although the difference in C_{PW}^a is large between schools 1 and 4, the C_{PW}^a of fish 4 in a triangular school is close to that in a diamond-shaped school with the same phase. This highlights the critical role of the body–body matching mechanism in power consumption.

To further investigate the body–body matching mechanism, the natural timeline is now considered, whereby the leading fish starts undulating at the same pose in different schools. The pressure fields of diamond-shaped and triangular schools with varied phases at $t = 0.25T$ are shown in Fig. 12. Compared with school 1 [Fig. 12(a)],

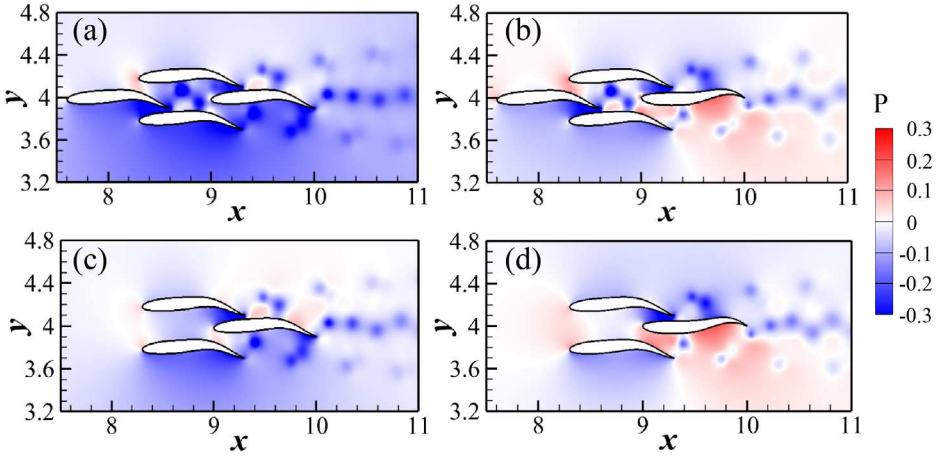

FIG. 12. Pressure field of (a) school 1 ($\varphi = 0°$), (b) school 4 ($\varphi = 270°$), (c) triangular school with $\varphi = 0°$, and (d) triangular school with $\varphi = 270°$ at $t = 0.25$.

school 4 exhibits higher pressure around the anterior part of fish 4 [Fig. 12(b)], while the triangular school at $\varphi = 0°$ has a similar pressure field [Fig. 12(c)], demonstrating that the body–body matching mechanism is essential to the hydrodynamics of the anterior part of fish 4 once again.

The instantaneous pressure around the anterior part of fish 4 depends on the lateral spacing and the relative motion between fish 4 and the channel, which changes dynamically with the phase difference. In Fig. 12(a), because of the difference in lateral spacing and relative motion, a negative pressure appears around the anterior part of fish 4 in school 1, and a high suction thrust is generated. In contrast, a positive pressure can be found at the same position on fish 4 in school 4, and a drag is produced. From a fluid dynamics standpoint, this phenomenon can be explained by momentum conservation law. In a high-density school, the phase difference determines the momentum flux passing by the anterior part of fish 4, thus controlling the net momentum transported downstream through the channel. According to Newton's second and third laws, the force generated by a fish is related to the momentum that the fish transfers to the downstream fluid.[41] That is, the matching between the channel and the anterior part of fish 4 governs its hydrodynamic performance. The phase difference effect on the hydrodynamics can then be revealed by comparing the momentum passing by the anterior part of fish 4 in schools 1 and 4.

Figure 13 presents the instantaneous streamwise momentum flux r_x at the inlet control surface (ICS) and outlet control surface (OCS) during one period for schools 1 and 4. The ICS is at the snout of fish 4, and the OCS is at the tail of fish 2 and fish 3, as shown in Figs. 13(a) and 13(b). In Fig. 13(c), the momentum flux at the ICSs is very similar in schools 1 and 4, with the time-averaged values of 0.057 and 0.052, respectively. This proves that other factors have only minor effects on the hydrodynamics of the channel. The momentum flux at the OCS r_{x_out} becomes much greater because of the energy output from fish 4 and the channel. We can see that r_{x_out} in school 1 is larger than that in school 4 over the whole period, and the time-averaged values are 0.093 and 0.076, respectively. Compared with $r^1_{x\_out}$, $r^4_{x\_out}$ is 18.7% lower. Figure 13(d) presents the net streamwise momentum flux over the volume bordered by the ICS and OCS, showing that Δr^1_x is larger than Δr^4_x during the whole period, and $\overline{\Delta r^1_x} = 0.037$ is 54.2% larger than $\overline{\Delta r^4_x} = 0.024$. The results indicate that, when changing the phase difference, Δr_x through the clearance between fish 4 and the channel may significantly increase because of the matching between fish 4 and the channel, leading to higher thrust production or lower energy consumption (or even the harvesting of energy from the flow) at the anterior part of fish 4. This effect of the phase difference is, thus, called the body–body matching mechanism.

D. Wake dynamics

The phase difference strongly influences the wake of a high-density diamond-shaped school. Figure 14 shows the representative vortex structures at $t = 10T$ and the mean flows of high-density fish schools with various phase differences. In Fig. 14, the three rows of vortex wakes are separately produced by the rear fish in each school. The 2P wakes[10] are produced by fish 2 and fish 3 on the upper and bottom rows, respectively, circled by blue dashed squares in Figs. 14(a1) and 15(a1). Due to symmetry, the upper and lower wake variations are similar, so only the upper wake is discussed below.

Although the wake pattern is maintained behind fish 2, the vortex strength, rotation angle, and advection velocity[37] of the vortex pairs change with the phase difference through the mutual interactions with the central wake produced by fish 4. In Figs. 14(a1)–14(f1), the fourth vortex pairs shed by fish 2, marked by P_{i4} in each figure ($i = a$–f denotes the figure number), are stable and have interacted with the

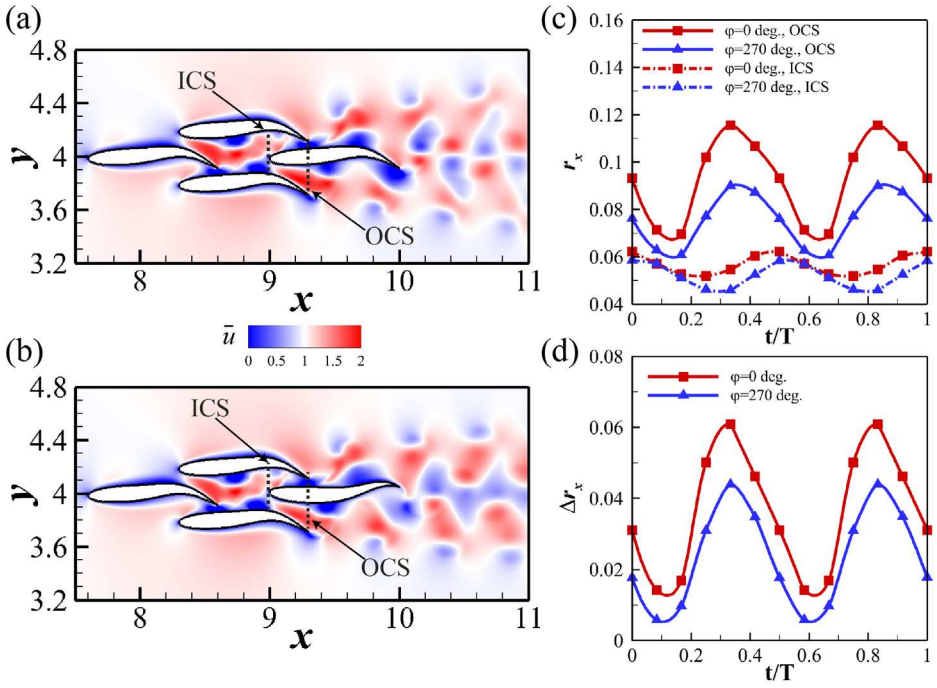

FIG. 13. (a) and (b) Streamwise velocity field, (c) momentum flux at ICS and OCS, and (d) net momentum flux of the channel for schools 1 and 4.

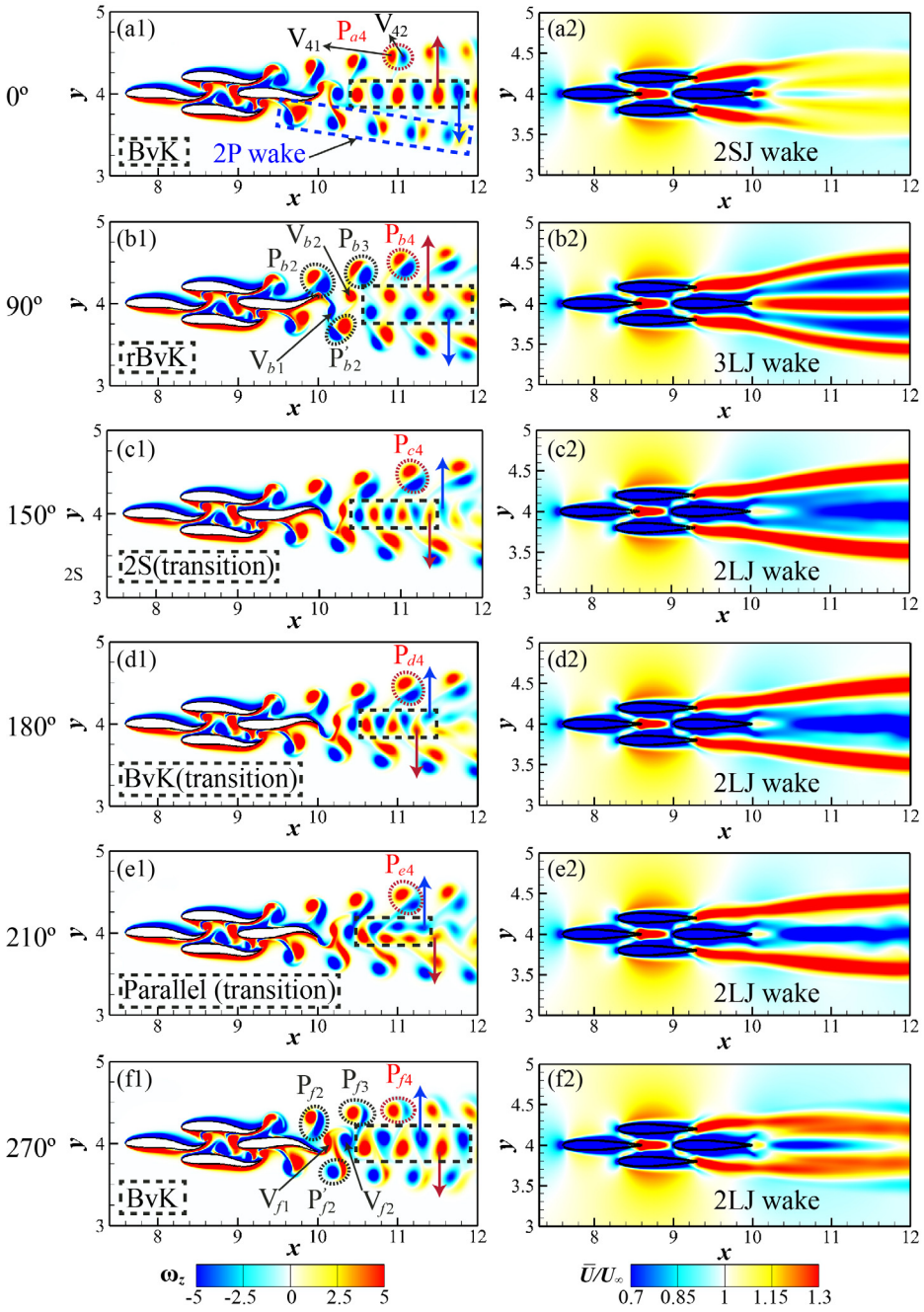

FIG. 14. Vortex wakes at $t = 10T$ (a1)–(f1) and the mean flow fields (a2)–(f2) of high-density schools at varied phase differences.

central wake over a period of time. Thus, we present the position, the rotation angle β, and the normalized circulation Γ^* of the fourth vortex pair P_4 in schools with varied phase differences at $t = 10T$ in Figs. 15(b)–15(d), respectively, to investigate the phase difference effects on the wake–wake interaction. The circulation is calculated by integrating the vorticity over an area A bounded by a predefined vorticity threshold ($\omega_z = 1$ for the positive vortex and $\omega_z = -1$ for the negative vortex), as shown in Fig. 15(a), and is normalized by the product of the incoming flow velocity U_∞ and the body length L.[37,42,43] The calculation of Γ^* can be expressed as follows:

$$\Gamma^* = \left|\frac{\Gamma}{U_\infty L}\right| = \left|\frac{1}{U_\infty L}\int\int_A \omega_z \cdot dA\right|, \tag{7}$$

where ω_z is the vorticity and A is the region enclosing vorticity above or below the threshold value.

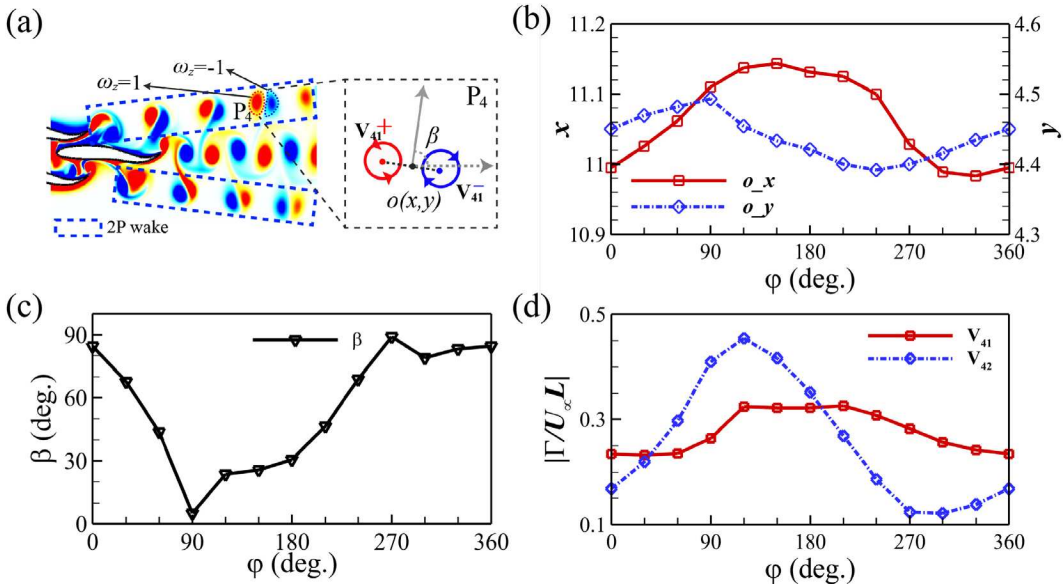

FIG. 15. (a) Schematic of the location o, rotation angle β and circulation calculation for a vortex pair, (b) relationship between the coordinates of vortex pair P_4 and the phase difference, (c) rotation angle of the vortex pair P_4 with respect to phase difference, and (d) absolute circulation of vortex 1 (V_{41}) and vortex 2 (V_{42}) in the pair P_4 varying with the phase difference.

Figure 16(b) shows the variation in the lateral spacing Δy between neighboring positive and negative vortices shed by fish 4, $\Delta y = y_{red} - y_{blue}$, where y_{red} and y_{blue} are located at the cores[37] of positive and negative vortices, respectively. For accuracy, we average the lateral spacings of three successive vortex pairs, circled by black dashed squares in Figs. 14(a1)–14(f1), to calculate Δy. The associated schematic of the calculation is shown in Fig. 16(a). The value of Δy indicates the patterns of the central wake produced by fish 4: when $\Delta y = 0$, it is a 2S aligned wake [see Fig. 14(c1)]; when $\Delta y > 0$, it is a 2S reversed Bénard–von Kármán (rBvK) vortex wake, as shown in Fig. 14(b1); when $\Delta y < 0$, it is a 2S Bénard–von Kármán (BvK) wake, as shown in Figs. 14(a1) and 14(f1).[44] The central wake produced by fish 4 could be at a transitional state, such as the parallel wake shown in Fig. 14(e1).

When $0° \leq \varphi < 90°$, the vortex pairs rotate clockwise, and the vortex wake strengthens with increasing phase difference, as shown in Figs. 14(a1) and 14(b1). The variations are quantitively shown in Fig. 15. Because the vortex pairs are shed at the same time and the same position in different schools, the larger coordinates in Fig. 15(b) imply a faster advection velocity for a vortex pair. It can be seen that the fourth vortex pair (P_4) in the school with a larger phase difference moves faster both in the streamwise and lateral directions. Additionally, Fig. 15(c) indicates that the vortex pair angle of P_4 reaches a minimum ($\beta_{min} = 5.05°$) at $\varphi = 90°$. The enhancement in the circulation and advection velocity of vortex pairs results in the augmentation of the mean flow behind fish 2. Simultaneously, the positive vortices in the central wake move upward, and the negative vortices move downward. Thus, the central wake transfers from the BvK pattern to the rBvK pattern, and the mean flow at the center is strengthened. Correspondingly, the mean flow of the school alters from a two-short-jet (2SJ) wake [Fig. 14(a2)] to a stronger three-long-jet (3LJ) wake [Fig. 14(b2)].

When increasing φ to 120°, the strength of the vortex pair P_4 is enhanced and reaches a maximum at $\varphi = 120°$, as shown in Fig. 15(d).

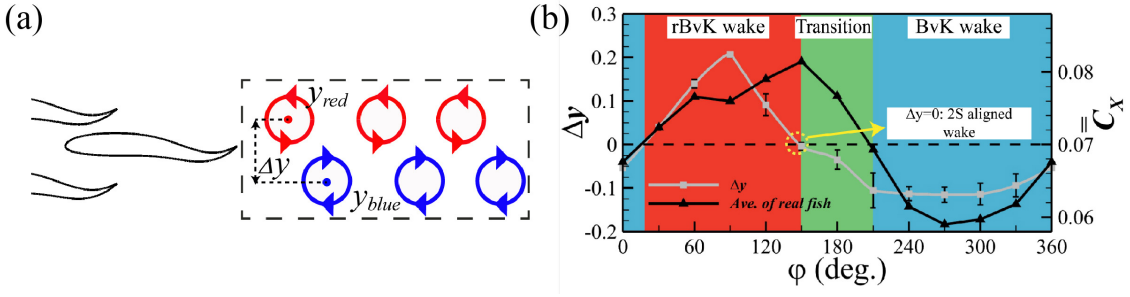

FIG. 16. (a) Schematic of the calculation of lateral spacing Δy between neighboring positive and negative vortices. (b) Central vortex wake and hydrodynamic performance of rear fish varying with the phase difference.

When $120^\circ \leq \varphi < 150^\circ$, Δy decreases as φ increases, indicating that the central wake becomes narrower. This results in a weaker rBvK wake in the center and stronger interaction between the negative vortices in the upper wake and the central wake. The negative vortices in the upper wake thus become weaker and stretched, as shown in Fig. 14(c1). Driven by the mutual induction between V_{41} and V_{42}, the vortex pair rotates counterclockwise and β increases [Fig. 15(c)]. When $\varphi = 150^\circ$, $\Delta y \approx 0$ and a 2S aligned wake is generated in the central region. Accordingly, the mean flow transfers to a two-long-jet (2LJ) wake [Fig. 14(c2)]. When $150^\circ \leq \varphi < 210^\circ$, the vortices produced by fish 4 cross the central line and move in the opposite spanwise directions. The central wake is transitional, changing from the rBvK type to the BvK type, and is unstable. The wake is of the BvK pattern at $\varphi = 180^\circ$, while it has changed to a "parallel" wake at $\varphi = 210^\circ$, as shown in Fig. 14(e1). Increasing the phase difference further, the center wake becomes a stable BvK type [Fig. 14(f1)]. Moreover, the lateral jet moves closer to the streamwise direction, but its strength decreases.

The above discussion suggests that phase difference greatly influences the wake pattern and the corresponding mean flow pattern of a high-density school. The associated mechanism is as follows. First, following the vortex pairing mechanism proposed in Ref. 10, vortex pairs are generated by fish 2 and fish 3 in a high-density school. During advection to downstream, the vortex pairs first interact with the undulating body of fish 4 (vortex–body interaction) and then are influenced by the shedding vortices of fish 4 (wake–wake interaction). In Fig. 14(b1), the vortices in vortex pair P_{b2} are strong and coherent, while in Fig. 14(f1), at the same position, the negative vortex in vortex pair P_{f2} is stretched and weakened due to the interaction with the body of fish 4, resulting in P_{f2} rotating counterclockwise. Next, the mutual interaction between the vortex pairs and the shedding vortices of fish 4, that is, the wake–wake interaction takes effect. The variation of vortex pair P_4 with respect to the phase difference shown in Figs. 15(b)–15(d) suggests that the wake–wake interaction can further influence the lateral wakes. In addition, the shedding vortices of fish 4 are also influenced by the wake–wake interaction. In the synchronized school ($\varphi = 0^\circ$), a 2S BvK wake is produced behind fish 4. Then, when increasing the phase difference, the negative vortex V_{b1} is moving downward, attracted by vortex pair P'_{b2} at the bottom, while the positive vortex V_{b2} is moving upward, attracted by vortex pair P_{b3} at the upper layer, as shown in Fig. 14(b1). An rBvK wake is thus formed. Continuing to increase the phase difference, the situation is reversed, and a BvK wake is then formed, as shown in Fig. 14(f1). The lateral motion of the shedding vortices of fish 4 depends on the relative distance to the vortex pairs, determined by the phase difference. The mechanism controlling the vortex dynamics indicates that the phase difference determines the wake pattern of a school.

In addition, the wake structures provide an indication of the hydrodynamic performance of a school. Based on the previous analysis, the swimming performance and vortex structure strongly depend on the phase difference. Thus, the relationship between vortex wake and performance can be determined through the phase difference. To help understand this relationship, we show the averaged $\overline{C_X}$ of the three-rear fish, which are directly related to the wake pattern in a school, $\overline{\overline{C_X}} = \sum_{i=2}^{4} \overline{C_X^i}/3$, where i denotes the fish number, as a function of phase difference in Fig. 16(b). Like the variation of Δy, the function has an approximately sinusoidal shape. When increasing φ ($<150^\circ$), Δy increases, and an rBvK (thrust-producing) wake is formed. Accordingly, a 2SJ mean flow wake gradually becomes a 3LJ wake [Fig. 14(b2)], implying more net thrust has been produced. Then, Δy starts to decline with increasing φ above 90°, and the thrust-producing wake becomes weaker. In contrast, due to the vortex induction and merging, more of the flow in the low-energy zone (the central wake) is transported to the high-energy wake (the 2P wake), and the lateral mean flow wake is strengthened. Thus, the $\overline{\overline{C_X}}$ continues to increase and reaches a maximum at $\varphi = 150^\circ$, $\overline{\overline{C_X}}_{\max} = 0.081$. The central wake then transforms from thrust-producing (rBvK wake) to drag-producing (BvK wake), and the flow is transported from the high-energy zone to the low-energy zone. Although the lateral jets are gradually deflected to the center, they have less strength and the $\overline{\overline{C_X}}$ drops. The subsequent development of the BvK wake and the force changes in a similar way as that of the rBvK wake with increasing φ. In summary, this study proves that the thrust–drag wake theory still provides an indication of the performance of multiple undulating body systems, and wake–wake interactions in the system can be elucidated by the flow transportation between low- and high-energy zones.

V. CONCLUSION

In this work, the sharp interface immersed boundary method has been applied to study the phase difference effects on the hydrodynamic interactions in high-density schools, including vortex–body, body–body, and wake–wake interactions. It has been found that the highest net thrust $\overline{C_{X\_\max}^{\text{ave.}}} = 0.08$, and the highest swimming efficiency, $\eta_{\max}^{\text{ave.}} = 0.57$, of the whole school can be achieved when the phase difference is 180°. The highest propulsive efficiency of fish 4 can be reached at $\varphi = 90^\circ$, where $\eta_{\max}^4 = 0.698$, an improvement of 58.3% over a single fish. At the same time, $\overline{C_T^4} = 0.376$ is 71.7% higher than $\overline{C_T}$ of a single fish. In addition, for fish 4, there exists a cosinusoidal relationship between $\overline{C_{PW}^4}$ and the phase difference and an approximately sinusoidal relationship between the swimming efficiency and the phase difference.

Based on its position in a school, the body of fish 4 was divided into two parts: (1) the anterior part, which lies in the channel formed by fish 2 and fish 3, and (2) the posterior part, which is outside of this channel. The associated mechanisms have been explored separately. For the posterior part of fish 4, the hydrodynamic performance in school 1 ($\varphi = 0^\circ$) and school 2 ($\varphi = 90^\circ$) were studied in detail. The vortex-capturing mechanism for an undulating body operates by choosing the appropriate phase, whereby the undulating body can produce more thrust and capture the energy from the vortex flow. Additionally, when vortices interact with the undulating body, the secondary vortex might attach to the body and advect downstream, thus enhancing thrust production or reducing power consumption by altering the pressure around the body. For the anterior part, the hydrodynamic performance in schools 1 and 4 ($\varphi = 270^\circ$) was compared to clarify the associated mechanisms. C_X and C_{PW} of the anterior part were calculated and quantitatively analyzed. The results suggest that the anterior part of fish 4 in school 1 can produce 56.3% more thrust than in school 4, while the anterior part in school 4 harvests energy from the flow instead of consuming power. By calculating the net streamwise momentum flux, we uncovered the body–body matching mechanism between the anterior part and the channel: by altering the phase, the anterior part can actively control the momentum flux that passes through the channel, resulting in improved thrust production or reduced energy consumption. The vortex-capturing mechanism

and body–body matching mechanism of the trailing fish in a high-density school will offer new insight into possible control strategies for efficient bio-inspired underwater robotic swarms and contribute to the understanding of the underlying physical mechanisms in fish schools.

Finally, the wake patterns of multiple undulating swimmer systems have been categorized and analyzed for the first time. A study of the vortex dynamics shows that the wake pattern of a school is strongly dependent on the phase difference. When increasing the phase difference from 0° to 360°, the vortex wake of fish 4 changes from the rBvK pattern to the BvK pattern due to the wake–wake interaction with the lateral wakes. Meanwhile, the vortex strength, rotation angle, and advection velocity of vortex pairs behind fish 2 and 3 vary with the phase difference because of the associated vortex–body and wake–wake interactions. Also, the relationship between the generated wake pattern and the performance of a high-density fish school has been built through the phase difference. This increased understanding of the wake dynamics of dense fish schools can inspire the accurate wake detection of multiple swimmers.

ACKNOWLEDGMENTS

This work was supported by NSF under No. CNS-1931929 and ONR MURI under Grant No. N00014-14-1-0533. Additionally, thanks to the University of Virginia Research Computing Group for the availability of the Rivanna supercomputing cluster.

AUTHOR DECLARATIONS

Conflict of Interest

The authors have no conflicts to disclose.

Author Contributions

Yu Pan: Conceptualization (equal); Data curation (lead); Formal analysis (lead); Investigation (lead); Methodology (equal); Validation (lead); Visualization (lead); Writing – original draft (lead); Writing – review and editing (equal). **Haibo Dong**: Conceptualization (equal); Funding acquisition (lead); Methodology (equal); Resources (lead); Project administration (lead); Supervision (lead); Writing – review and editing (equal).

DATA AVAILABILITY

The data that support the findings of this study are available from the corresponding author upon reasonable request.

REFERENCES

[1]D. Weihs, "Hydromechanics of fish schooling," Nature **241**, 290 (1973).
[2]S. Marras, S. S. Killen, J. Lindström, D. J. McKenzie, J. F. Steffensen, and P. Domenici, "Fish swimming in schools save energy regardless of their spatial position," Behav. Ecol. Sociobiol. **69**, 219 (2015).
[3]J. Herskin and J. F. Steffensen, "Energy savings in sea bass swimming in a school: Measurements of tail beat frequency and oxygen consumption at different swimming speeds," J. Fish Biol. **53**, 366 (1998).
[4]S. S. Killen, S. Marras, J. F. Steffensen, and D. J. McKenzie, "Aerobic capacity influences the spatial position of individuals within fish schools," Proc. R. Soc. Biol. Sci. **279**, 357 (2012).
[5]J. C. Liao, D. N. Beal, G. V. Lauder, and M. S. Triantafyllou, "Fish exploiting vortices decrease muscle activity," Science **302**, 1566 (2003).
[6]J. C. Liao, D. N. Beal, G. V. Lauder, and M. S. Triantafyllou, "The Karman gait: Novel body kinematics of rainbow trout swimming in a vortex street," J. Exp. Biol. **206**, 1059 (2003).
[7]B. M. Boschitsch, P. A. Dewey, and A. J. Smits, "Propulsive performance of unsteady tandem hydrofoils in an in-line configuration," Phys. Fluids **26**, 051901 (2014).
[8]R. Gopalkrishnan, M. S. Triantafyllou, G. S. Triantafyllou, and D. Barrett, "Active vorticity control in a shear flow using a flapping foil," J. Fluid Mech. **274**, 1 (1994).
[9]A. P. Maertens, A. Gao, and M. S. Triantafyllou, "Optimal undulatory swimming for a single fish-like body and for a pair of interacting swimmers," J. Fluid Mech. **813**, 301 (2017).
[10]Y. Pan and H. Dong, "Computational analysis of hydrodynamic interactions in a high-density fish school," Phys. Fluids **32**, 121901 (2020).
[11]P. A. Dewey, D. B. Quinn, B. M. Boschitsch, and A. J. Smits, "Propulsive performance of unsteady tandem hydrofoils in a side-by-side configuration," Phys. Fluids **26**, 041903 (2014).
[12]G.-J. Dong and X.-Y. Lu, "Characteristics of flow over traveling wavy foils in a side-by-side arrangement," Phys. Fluids **19**, 057107 (2007).
[13]L. Li, M. Nagy, J. M. Graving, J. Bak-Coleman, G. Xie, and I. D. Couzin, "Vortex phase matching as a strategy for schooling in robots and in fish," Nat. Commun. **11**, 5408 (2020).
[14]I. Akhtar, R. Mittal, G. V. Lauder, and E. Drucker, "Hydrodynamics of a biologically inspired tandem flapping foil configuration," Theor. Comput. Fluid Dyn. **21**, 155 (2007).
[15]T. M. Broering, Y. Lian, and W. Henshaw, "Numerical investigation of energy extraction in a tandem flapping wing configuration," AIAA J. **50**, 2295 (2012).
[16]M. Kurt and K. W. Moored, "Flow interactions of two-and three-dimensional networked bio-inspired control elements in an in-line arrangement," Bioinspiration Biomimetics **13**, 045002 (2018).
[17]R. Godoy-Diana, J. Vacher, V. Raspa, and B. Thiria, "On the fluid dynamical effects of synchronization in side-by-side swimmers," Biomimetics **4**, 77 (2019).
[18]Y. Bao, D. Zhou, J. Tao, Z. Peng, H. Zhu, Z. Sun, and H. Tong, "Dynamic interference of two anti-phase flapping foils in side-by-side arrangement in an incompressible flow," Phys. Fluids **29**, 033601 (2017).
[19]M. Kurt, A. Eslam Panah, and K. W. Moored, "Flow interactions between low aspect ratio hydrofoils in in-line and staggered arrangements," Biomimetics **5**, 13 (2020).
[20]C. K. Hemelrijk, D. A. P. Reid, H. Hildenbrandt, and J. T. Padding, "The increased efficiency of fish swimming in a school," Fish Fish. **16**, 511 (2015).
[21]M. Daghooghi and I. Borazjani, "The hydrodynamic advantages of synchronized swimming in a rectangular pattern," Bioinspiration Biomimetics **10**, 056018 (2015).
[22]S. Y. Chen, Y. H. J. Fei, Y. C. Chen, K. J. Chi, and J. T. Yang, "The swimming patterns and energy-saving mechanism revealed from three fish in a school," Ocean Eng. **122**, 22 (2016).
[23]A. U. Oza, L. Ristroph, and M. J. Shelley, "Lattices of hydrodynamically interacting flapping swimmers," Phys. Rev. X **9**, 041024 (2019).
[24]M. Gazzola, A. A. Tchieu, D. Alexeev, A. de Brauer, and P. Koumoutsakos, "Learning to school in the presence of hydrodynamic interactions," J. Fluid Mech. **789**, 726 (2016).
[25]S. Verma, G. Novati, and P. Koumoutsakos, "Efficient collective swimming by harnessing vortices through deep reinforcement learning," Proc. Natl. Acad. Sci. U. S. A. **115**, 5849 (2018).
[26]S. Alben, "Collective locomotion of two-dimensional lattices of flapping plates. Part 2. Lattice flows and propulsive efficiency," J. Fluid Mech. **915**, A21 (2021).
[27]A. Filella, F. Nadal, C. Sire, E. Kanso, and C. Eloy, "Model of collective fish behavior with hydrodynamic interactions," Phys. Rev. Lett. **120**, 198101 (2018).
[28]P. Han, Y. Pan, G. Liu, and H. Dong, "Propulsive performance and vortex wakes of multiple tandem foils pitching in-line," J. Fluids Struct. **108**, 103422 (2022).
[29]R. Mittal, H. Dong, M. Bozkurttas, F. Najjar, A. Vargas, and A. Von Loebbecke, "A versatile sharp interface immersed boundary method for incompressible flows with complex boundaries," J. Comput. Phys. **227**, 4825 (2008).

[30]G. Liu, Y. Ren, H. Dong, O. Akanyeti, J. C. Liao, and G. V. Lauder, "Computational analysis of vortex dynamics and performance enhancement due to body–fin and fin–fin interactions in fish-like locomotion," J. Fluid Mech. **829**, 65 (2017).
[31]P. Han, G. V. Lauder, and H. Dong, "Hydrodynamics of median-fin interactions in fish-like locomotion: Effects of fin shape and movement," Phys. Fluids **32**, 011902 (2020).
[32]G. Novati, S. Verma, D. Alexeev, D. Rossinelli, W. M. van Rees, and P. Koumoutsakos, "Synchronisation through learning for two self-propelled swimmers," Bioinspiration Biomimetics **12**, 036001 (2017).
[33]I. Borazjani and F. Sotiropoulos, "Numerical investigation of the hydrodynamics of carangiform swimming in the transitional and inertial flow regimes," J. Exp. Biol. **211**, 1541 (2008).
[34]W. W. Schultz and P. W. Webb, "Power requirements of swimming: Do new methods resolve old questions?," Integr. Comp. Biol. **42**, 1018 (2002).
[35]A. P. Maertens, M. S. Triantafyllou, and D. K. Yue, "Efficiency of fish propulsion," Bioinspiration Biomimetics **10**, 046013 (2015).
[36]T. Ming, B. Jin, J. Song, H. Luo, R. Du, and Y. Ding, "3D computational models explain muscle activation patterns and energetic functions of internal structures in fish swimming," PLoS Comput. Biol. **15**, e1006883 (2019).
[37]R. Godoy-Diana, C. Marais, J.-L. Aider, and J. E. Wesfreid, "A model for the symmetry breaking of the reverse Bénard–von Kármán vortex street produced by a flapping foil," J. Fluid Mech. **622**, 23 (2009).
[38]O. R. Burggraf, "Analytical and numerical studies of the structure of steady separated flows," J. Fluid Mech. **24**, 113 (1966).
[39]L. Kang, Z.-R. Peng, H. Huang, X.-Y. Lu, and W. Cui, "Active external control effect on the collective locomotion of two tandem self-propelled flapping plates," Phys. Fluids **33**, 101901 (2021).
[40]L. Kang, W. Cui, X.-Y. Lu, and H. Huang, "Hydrodynamic force induced by vortex–body interactions in orderly formations of flapping tandem flexible plates," Phys. Fluids **34**, 021901 (2022).
[41]J. O. Dabiri, "On the estimation of swimming and flying forces from wake measurements," J. Exp. Biol. **208**, 3519 (2005).
[42]A. T. Bode-Oke, S. Zeyghami, and H. Dong, "Flying in reverse: Kinematics and aerodynamics of a dragonfly in backward free flight," J. R. Soc. Interface **15**, 20180102 (2018).
[43]M. S. U. Khalid, J. Wang, I. Akhtar, H. Dong, M. Liu, and A. Hemmati, "Why do anguilliform swimmers perform undulation with wavelengths shorter than their bodylengths?," Phys. Fluids **33**, 031911 (2021).
[44]T. Schnipper, A. Andersen, and T. Bohr, "Vortex wakes of a flapping foil," J. Fluid Mech. **633**, 411 (2009).